Title

Experimental and theoretical thermal analysis of a Hybrid Silicon Evanescent Laser

Journal

Optics Express, 15(23)

Authors

Sysak, Matthew

Bowers, J E

Publication Date

2007-10-30

Peer reviewed

Experimental and theoretical thermal analysis of a Hybrid Silicon Evanescent Laser

Matthew N. Sysak[1], Hyundai Park[2], Alexander W. Fang[2], John E. Bowers[2], Richard Jones[1], Oded Cohen[3], Omri Raday[3], Mario Paniccia[1]

[1]Intel Corporation, 2200 Mission College Blvd. SC12-236 Santa Clara, Ca 95054, USA
[2]Electrical and Computer Engineering, University of California, Santa Barbara, CA 93106, USA
[3]Intel Corporation, S.B.I. Park Har Hotzvim, Jerusalem, 91031, Israel

matthew.n.sysak@intel.com

Abstract: In this work we present both experimental and theoretical thermal analysis of an electrically pumped hybrid silicon evanescent laser. Measurements of an 850 μm long Fabry-Perot structure show an overall characteristic temperature of 51 ^{o}C, an above threshold characteristic temperature of 100 ^{o}C, and a thermal impedance of 41.8 ^{o}C/W. Finite element analysis of the laser structure predicts a thermal impedance of 43.5 ^{o}C/W, which is within 5% of the experimental results. Using the overall characteristic temperature, above threshold characteristic temperature, and the measured thermal impedance, the continuous wave output power vs. current from the laser is simulated and is in good agreement with experiment.

OCIS codes: (140.5960) Lasers and laser optics; (060.2340) Fiber optics components

References and links

1. H. Rong, R. Jones, A. Liu, O. Cohen, D. Hak, A. W. Fang, and M. Paniccia, "A continuous-wave Raman silicon laser," Nature **433**, 725-728 (2005).
2. S. G. Cloutier, P. A. Kossyrev, and J. Xu, "Optical gain & stimulated emission in periodic nanopatterned crystalline silicon," Nat. Materials **4**, 887 (2005).
3. S. Lombardo, S. U. Campisano, G. N. van den Hoven, A Cacciato, A. Polman, "A Room-temperature luminescence from Er3+-implanted semi-insulating polycrystalline silicon," Appl. Phys. Lett. **63**, 1942–1944 (1993).
4. A. W. Fang, R. Jones, H. Park, O. Cohen, O. Raday, M. J. Paniccia, and J. E. Bowers, "Integrated AlGaInAs-silicon evanescent race track laser and photodetector," Opt. Express **5**, 2315-2322, (2007).
5. L. Coldren and S. Corzine, "Diode Lasers and Photonic Integrated Circuits," New York: Wiley 1995.
6. S. Aadachi, "Lattice thermal resistivity of III-V compound alloys," J. Appl. Phys. **54**, 1844-1848 (1983).
7. E, Kapon, "Semiconductor Lasers II (Materials and Structures)," San Diego: Academic Press, 2005.
8. J. Piprik, J. Kenton White, A.J. SpringThorpe, "What Limits the Maximum Output Power of Long-Wavelength AlGaInAs/InP Laser Diodes?" IEEE J. Quantum Electron. **38**, 1253-1259 (2002).

I. Introduction

Recently, there has been significant interest in developing a laser source that is compatible with silicon based optics and electronics. A laser that can be integrated with silicon optical and electrical components has the potential to utilize the low cost, high volume manufacturing that has been developed in the CMOS microelectronics industry. Several optical sources that could fulfill this requirement have been proposed and demonstrated. These include optically pumped Raman lasers [1], nano-crystalline Si structures [2], and rare-earth doped Si rich oxides [3]. Of these integrated solutions, one of the most attractive is a wafer bonded hybrid silicon laser. In this approach, a III-V active region is wafer bonded onto a pre-patterned silicon on insulator (SOI) wafer. Lasers fabricated in this manner do not require aligned bonding steps since the optical waveguides are defined in the silicon. Furthermore, these lasers can be integrated with additional passive and active components such waveguide splitters, waveguide combiners, evanescent photodetectors, and amplifiers. Using the wafer bonded approach, Fabry-Perot (FP) and ring lasers have demonstrated output powers greater

than 20 mW, threshold currents of < 75 mA and operating temperatures up to 60 ^{o}C [4]. Unfortunately, one of the drawbacks to fabricating integrated lasers using an SOI substrate deals with the ability of the device to dissipate heat. While crystalline silicon is a good thermal conductor (thermal conductivity, k_{Si} ~ 130 W/m/K), the oxide in the SOI substrate has poor thermal conductivity (k_{SiO2} ~ 1.3 W/m/K). The poor thermal properties of the buried oxide layer represent an issue for high temperature laser performance.

In this work, we present experimental and theoretical thermal analysis of a hybrid silicon evanescent Fabry-Perot (FP) laser. For an 850 μm long device, measurements show an overall characteristic temperature (T_0) of 51 ^{o}C, an above threshold characteristic temperature (T_1) of 100 ^{o}C, and a thermal impedance (Z_T) of 41.8 ^{o}C/W. Simulations of the thermal impedance in the hybrid laser using a finite element modeling technique predicts a Z_T of 43.5 ^{o}C/W, which is within 5% of the experimental results. Using the theoretical model it is shown that the buried oxide in the SOI substrate accounts for 25.2 ^{o}C/W of the total device thermal impedance. Combining the experimental T_0, T_1, and Z_T, the relationship between the continuous wave (CW) output power from the laser and applied current at various backside temperatures is predicted. For temperatures of 15 ^{o}C, 25 ^{o}C, and 35 ^{o}C, the agreement between the theoretical and experimental laser characteristics is good, but the agreement is worse at higher temperatures for reasons discussed in Section VI.

II. Device overview

The hybrid silicon evanescent laser consists of a III-V InGaAlAs/InP active region that is wafer bonded to a pre-patterned SOI wafer. A cross section of the device is shown in Fig. 1.

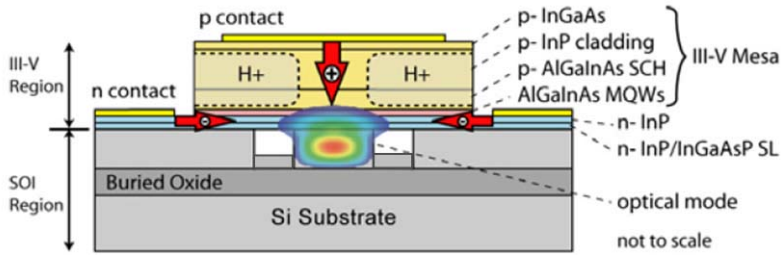

Fig. 1. Schematic of the wafer bonded hybrid evanescent laser structure. Current is injected in the laser active region from the top p contacts and the side n-contacts.

Device fabrication begins by patterning a set of rib waveguides on an SOI wafer. The rib etch depth is 0.5 μm and the waveguide with is 2 μm. Following the silicon patterning, a plasma assisted wafer bonding process is performed to bond an InGaAlAs/InP active region to the SOI wafer. No alignment steps are required in the bonding process. Following the bonding, additional fabrication steps are performed including removal of the InP substrate, dry etch definition of the III-V mesas, proton (H+) implantation of the p-InP cladding (for current confinement), and definition of the p and n contact regions. A detailed description of the fabrication process can be found in [4]. For testing, the FP lasers were diced into bars of 32 devices (bar dimension 850 μm x 8 mm) and facets were polished.

III. Hybrid laser characteristic temperatures

The threshold current and differential efficiency of the hybrid laser at elevated temperatures can be characterized using an overall characteristic temperature (T_0) and an above threshold characteristic temperature (T_1) [5]. These characteristic temperatures are described in Eq. (1) and Eq. (2), where I_0 and I_{PO} are fitting parameters.

$$I_{th} = I_0 e^{T/T_0} \tag{1}$$

$$I - I_{th} = I_{P0} e^{T/T_1} \tag{2}$$

To extract the two characteristic temperatures, a set of pulsed output power vs. applied current (LI) measurements (1 kHz repetition rate, 0.1% duty cycle) were performed with the device placed on a temperature controlled stage. The pulsed measurement ensures that there is limited additional heating from power dissipation in the laser other than that provided by the stage. Thermal paste was used for efficient heat conduction between the lasers and the stage. LI results from these measurements are shown in Fig. 2 for stage temperatures ranging from 20 to 45 ^{o}C. Using Eqn. (1), T_0 and I_0 can be extracted by fitting the natural log of threshold current vs. the stage temperature. Results are shown in Fig. 3(a) and give an overall characteristic temperature of 51 ^{o}C and an I_0 of 48 mA. Fitting the difference in current between threshold and that required for 1 mW of output power allows the above characteristic temperature to be determined. Results are shown in Fig. 3(b) and yield a T_1 of 100 ^{o}C with an I_{p0} of 10.65 mA.

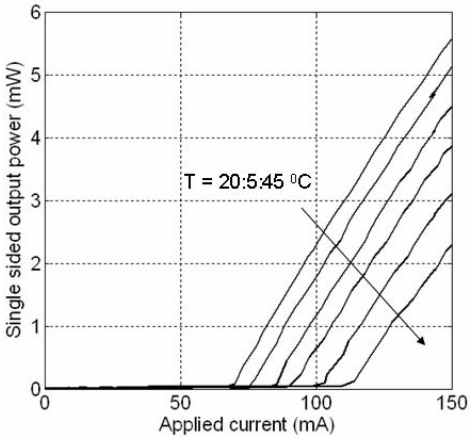

Fig. 2. Single facet pulsed LI measurements for the 850 μm long FP hybrid laser. Results are shown for stage temperatures between 20 to 45 ^{o}C and are in 5 ^{o}C steps.

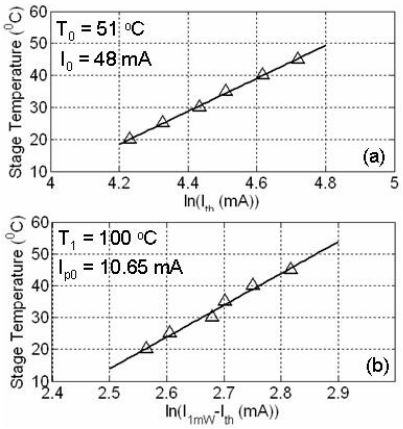

Fig. 3.(a) Natural log of I_{th} as a function of stage temperature. (b) Natural log of the current required above threshold for an output power of 1 mW .

IV. Experimental thermal impedance

The thermal imepdance of the laser is measured using a combination of two experiments. The first set of measurements is used to establish a baseline for the shift in lasing wavelength as a function of active region (stage) temperature ($d\lambda/dT$). Similar to the characteristic temperature measurement above, this experiment is performed pulsed to ensure that there is minimal device heating other than what is provided by the temperature controlled stage. The second measurement is performed CW, and is used to measure the shift in wavelength as a function of applied electrical power to the laser ($d\lambda/dP$). Z_T is then given by Eq. (3):

$$Z_T = \left(\frac{d\lambda}{dT}\right)^{-1}\left(\frac{d\lambda}{dP}\right) \tag{3}$$

The experimental shift in wavelength as function of stage temperature for the pulsed measurements, along with the output spectrum from the FP laser at 15 ^{o}C and 30 ^{o}C are shown in Fig. 4(a). For the CW measurements, the experimental shift in lasing wavelength is shown in Fig. 4(b). In all experiments, a single longitudinal mode in the laser spectrum is monitored. Combining the results in Fig. 4(a) and 4(b) results in a thermal impedance of 41.8 ^{o}C/W.

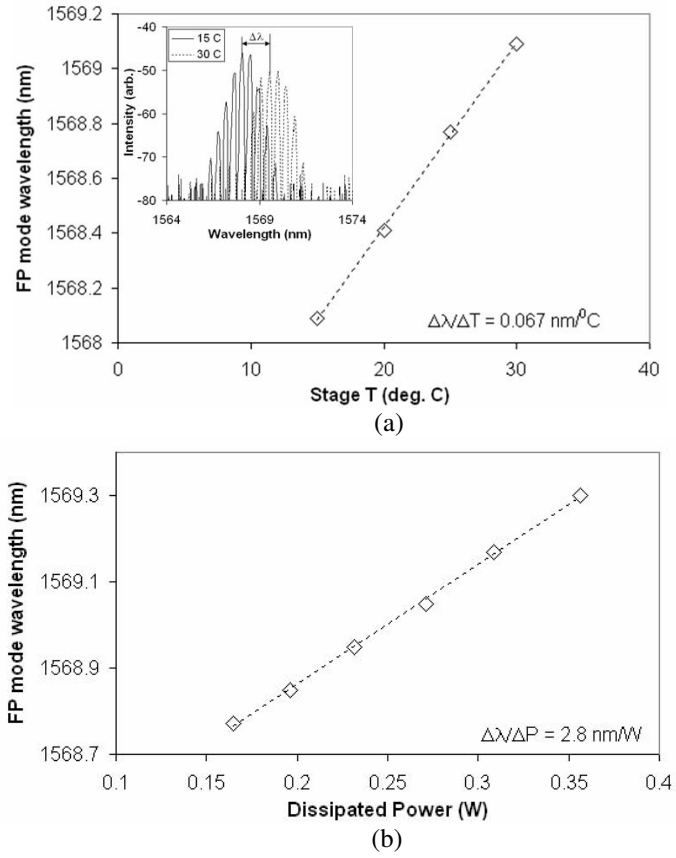

Fig. 4(a). Pulsed measurement results for the shift in lasing wavelength (single FP mode) as a function of stage temperature. The inset contains a laser output spectrum at 15 ºC and 30 ºC. (b) Results for the shift in lasing wavelength (single FP mode) as a function of dissipated power.

V. Theoretical thermal impedance

The thermal performance of the hybrid laser depends on several factors. These include the amount and location of heat that is generated, the thermal conductivity of the layers surrounding the heat sources, and the operating temperature of the laser active region. To model the temperature rise as a function of applied bias we have employed a two dimensional finite element modeling technique. For the hybrid laser cross section shown in Fig. 1, there are six major sources of thermal energy. These include resistive heating in the p-cladding, the n-contact layer, the active region, and the p and n contacts, along with heat generated by the diode drop associated with the active region. Although for shorter devices the contact resistance in the hybrid laser would be problematic, for an 850 μm long FP laser, the n and p contact resistance is not significant compared to that of the p-cladding and n-contact layers. Hence it is neglected in the model.

For the resistive heating, the resistances of the various laser regions (p-cladding, n-InP contact layer, etc.) have been extracted using transmission line measurements (TLM). Based on these measurements, an 850 μm long FP structure has a p-cladding resistance of 3.3 Ω and an n-contact layer resistance of 2.9 Ω. For the active region, the total resistance was calculated to be 0.3 Ω, and is based on the material resistivity for the average composition between the wells and barriers [6], the thickness of the active layer (0.1 μm), and the width of the unimplanted region (4 μm). The dissipated electrical power associated with resistive heating in the model is calculated by simply taking the product of the square of the current in a particular layer and the resistive contribution in each device section. For the dissipated

power in the n-InP contact layer, the current is reduced by a factor of two since the double sided n-contact shown in Fig 1 acts as a current divider. For the active region diode drop, the dissipated power is simply the turn on voltage multiplied by the current.

The dimensions of the hybrid laser used in the model are shown in Fig. 5. The thermal conductivity in each of the various regions is k_{InP} = 130 W/m/K, k_{Si} = 130 W/m/K, k_{SiO2} = 1.3 W/m/K, and k_{QWs} = 5 W/m/K (active QWs) [6].

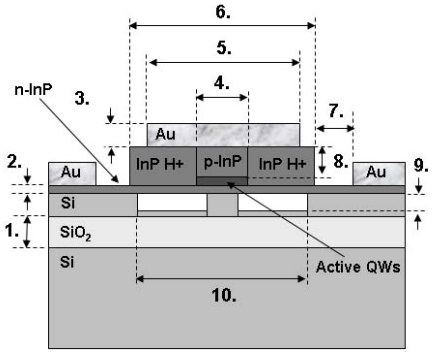

Layer	Description	Dimension
1	SiO_2 thickness	1.0 μm
2	n-InP contact layer	100 nm
3	P/N metal	1.5 μm
4	p-InP (no implant)	4 μm
5	P-metal width	8 μm
6	III-V mesa	12 μm
7	Metal separation	4 μm
8	InP cladding	2 μm
9.	Rib etch depth	0.5 μm
10.	Rib width	8 μm

Fig. 5. Detailed description of the device dimensions used in the finite element thermal model.

A two dimensional temperature profile of the hybrid laser operating with a bias current of 500 mA is shown in Fig. 6(a). The predicted temperature rise in the laser active region as a function of applied current, is shown in Fig. 6(b). Results show that for applied bias currents greater than 250 mA, the largest source of power dissipation is the p-cladding region, followed by the active region, then the n-InP layer. Using the simulated temperature rise and dissipated electrical power, the thermal impedance of the laser is 43.5 °C/W, which is within 5% of our initial experimental results.

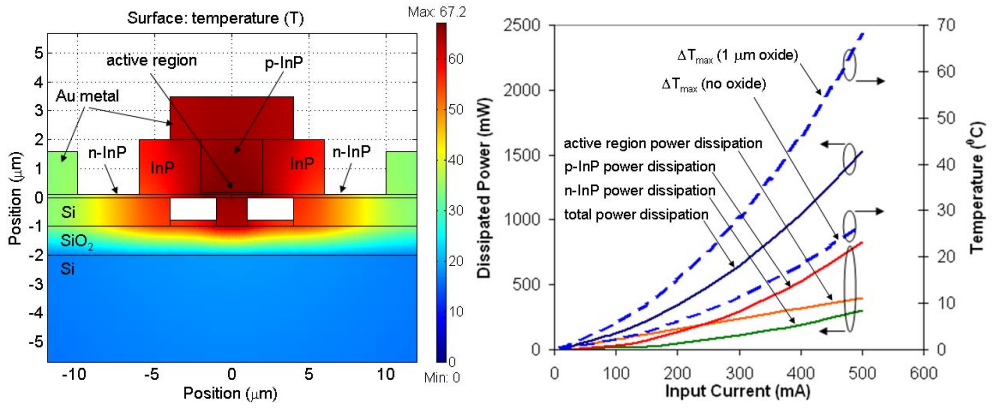

(a) (b)

Fig. 6. (a) Two dimensional temperature profile in the hybrid laser at a bias current of 500 mA. (b) Theoretical predictions for the dissipated electrical power in the various laser sections along with the predicted temperature rise in the active region as a function of contact current.

To show the effect of the buried oxide on the thermal impedance, Fig. 6(b) also includes a simulation of the temperature rise in the device when the buried oxide has been removed. Although removal of the BOX has adverse effects on the optical guiding characteristics of the laser, replacing this layer with silicon would result in a thermal impedance of 18.3 °C/W.

VI. Continuous wave LI experiments and theory

The characteristic temperatures in combination with the experimental and theoretical predictions of thermal impedance can be used to predict the CW LI properties of the laser as a

function of stage temperature [7]. Combining Eqn. 1 and Eqn. 2 [5], the output power (P_{out}) from the 850 μm long hybrid laser is given by Eq. (4).

$$P_{out} = \eta i \left(\frac{\alpha_m}{\langle \alpha_i \rangle + \alpha_m} \right) \left(\frac{h\nu}{q} \right) e^{((Z_T(P_D - Pout)+T)/T_1)} \left(I - I_0 e^{((Z_T(P_D - Pout)+T)/T_0)} \right) \quad (4)$$

In Eqn. 4, P_D is the total electrical power dissipation in the laser, I is the applied bias current, I_0 is the fitting parameter from Eqn 1, and η_i, α_m, hν, q and $<\alpha_i>$ have their typical definitions. Given an injection efficiency of 70%, a modal loss of 10 cm^{-1}, and an estimated mirror loss of 11.4 cm^{-1} (facet reflectivity 38%), Fig. 7(a) shows the predicted and experimental single sided laser output power (measured into an integrating sphere) at various backside temperatures. A set of residuals along with an R^2 value for each of the theoretical fits are shown in Fig. 7(b).

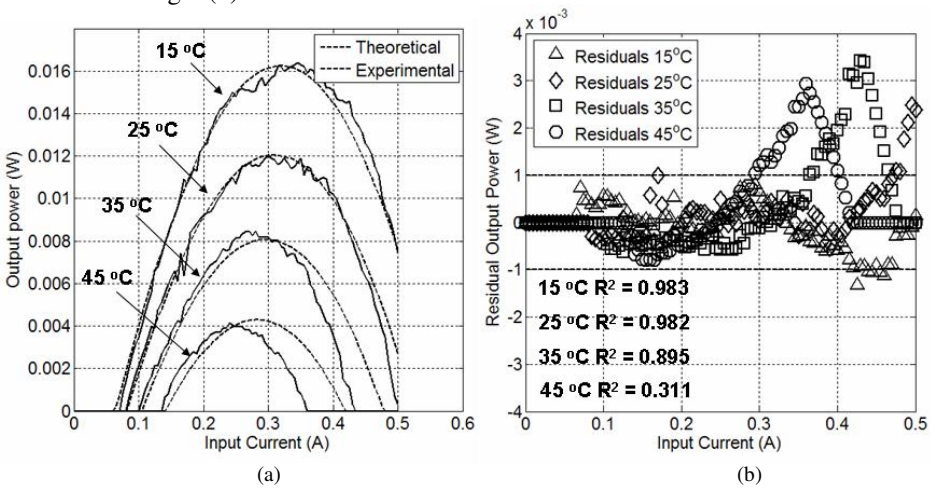

(a) (b)

Fig. 7. (a) CW LI experimental results (solid) and theoretical predictions (dashed) for the FP hybrid laser at backside temperatures between 15 and 45 ^{0}C. (b) Residual output power between theory and experiment.

For operating temperatures of 15 °C and 25 °C, R^2 values of 0.983 and 0.982 along with small residuals (<+/-1 mW) over >95% of the data indicates a good fit between theory and experiment. For temperatures of 35 °C and 45 °C, the decrease in the R^2 (0.895 and 0.311 respectively) and increase in residuals at high bias currents are most likely caused by thermal runaway effects that are not included in Eq. (4), but are described in [8].

VII. Conclusions

We have experimentally and theoretically investigated the thermal performance of a FP hybrid silicon evanescent laser. Experiments show a T_0 of 51 °C, T_1 of 100 °C, and a Z_T of 43.5 °C/W. Simulations of the laser using finite element analysis show a Z_T of 41.5 °C/W, which is within 5% of our experimental results. Using a combination of T_0, T_1, and Z_T, the laser output power vs. current characteristics are predicted and compared with experiment. At stage temperatures of 15 °C and 25 °C, there is good agreement between theory and experiment. At temperatures of 35 °C and 45 °C, degradation between the experimental and theoretical predictions occurs due to thermal runaway.